

We are IntechOpen, the world's leading publisher of Open Access books Built by scientists, for scientists

6,900

Open access books available

186,000

International authors and editors

200M

Downloads

Our authors are among the

154

Countries delivered to

TOP 1%

most cited scientists

12.2%

Contributors from top 500 universities



WEB OF SCIENCE™

Selection of our books indexed in the Book Citation Index
in Web of Science™ Core Collection (BKCI)

Interested in publishing with us?
Contact book.department@intechopen.com

Numbers displayed above are based on latest data collected.
For more information visit www.intechopen.com



Nanoplasmonic Waveguides Filled with Electro-Optical Materials

Montasir Qasymeh

Additional information is available at the end of the chapter

<http://dx.doi.org/10.5772/67370>

Abstract

In this chapter, nanoplasmonic waveguides filled with electro-optical materials are proposed and discussed. Rigorous theoretical modelling is developed to describe the propagation, generation and control of electromagnetic fields confined in these nanoscale waveguides. Two configurations are studied thoroughly. First, a metal-insulator-metal (MIM) nanoplasmonic waveguide filled with lithium niobate (i.e., LiNbO_3) is considered for compact terahertz (THz) generation. The waveguide is designed to generate Gaussian THz waves by the means of frequency down-conversion of two surface plasmon polariton (i.e., SPP) modes. THz generation is shown to be viable over the entire range from 1 to 10 THz by properly designing the SPP wavelengths and waveguide dimensions. Future applications of such nanoscale THz sources include nanocommunication systems and body-centric networks. Secondly, an MIM nanoplasmonic waveguide filled with doped LiNbO_3 is considered. The interaction between two interfering SPP modes is studied. It is shown that a strong symmetric SPP mode can be coupled to a weak antisymmetric SPP mode by the means of photorefractive effect. Future advances include implementing known photorefractive applications (such as interferometry and holography) in the nanoplasmonic field. The work of this chapter highlights the potential of functioning electro-optical materials in nanoplasmonic waveguides to achieve novel ultra-compact and efficient devices.

Keywords: plasmonic waveguides, electro-optic material, lithium niobate, terahertz, photorefractive effect

1. Introduction

Nanoplasmonic waveguides offer unprecedented tight confinement of electromagnetic waves in subwavelength structures. In principle, nanoplasmonic waveguides comprise several metal-dielectric layers. The propagating light is coupled to the free electrons in the metal, which acts like plasma at the optical frequency. It then follows that the propagating light can be strongly confined even to 100 times smaller than its wavelength. Such tight confinement has the potential to open a new world of scalability and integration. For instance, nanoplasmonic-based devices can be utilized as matching interconnectors between traditional micro-photonics and nanoelectronic devices [1–5]. This paves the way for the development of efficient, compatible and ultrafast chips [6–8]. However, the achievable tight confinement in the nanoplasmonic waveguides can be functioned to boost the propagating waves' intensities. It then follows that the nonlinear effects can be significantly enhanced, and thus, desired functionalities can be achieved. To date, several advances in plasmonic technology have been reported. These include all optical nanoplasmonic logic gates [9], electrically controlled plasmonic devices [10], plasmonic amplification and lasing [11], efficient second harmonic generation using plasmonic waveguides [12], silicon-on-insulator-compatible plasmonic devices [13], focus and enhancement of terahertz (THz) radiation using plasmonic waveguides [14], efficient and ultra-compact hybrid plasmonic devices [15], solitonic plasmonic waveguides [16] and mode conversion in plasmonic waveguides [17], to mention a few examples.

In this chapter, nanoplasmonic waveguides filled with electro-optical materials are proposed and discussed. Specifically, metal-insulator-metal (MIM) plasmonic waveguides filled with lithium niobate (LiNbO_3) are considered. The theoretical models that describe the nonlinear interaction of the confined electromagnetic waves in nanoplasmonic waveguides are developed. Numerical evaluations based on experimentally reported parameters are provided. Two different configurations are studied thoroughly. The first configuration is a MIM nanoplasmonic waveguide designed for compact THz generation [18]. The optical pumps are guided by means of surface plasmon polaritons (SPPs), whereas the generated THz waves are designed to diffract and propagate outside the MIM waveguide. The design of this work attains the following desired properties: first, the THz absorption is minimized. Secondly, the proposed structure is compact and relevant for nanoapplications. Thirdly, the generation efficiency is maximized by reducing losses rather than introducing resonant conditions (i.e. phase matching), and thus, wide THz generation is achieved. We note that this proposal introduces a new modality from the standpoint of applications. For instance, the proposed MIM nanostructure can be immersed inside a target (such as a cell or a biological entity), and the generated THz waves can interact with the (under-test) surrounding medium of the MIM nanostructure, while the optical modes are tightly confined inside the MIM nanostructure. Potential future applications include nanocommunication networks and body-centric systems. The second configuration considered in this work includes MIM plasmonic waveguide filled with doped LiNbO_3 [19]. The main interest is to study the interaction of the interfering SPP modes with the doping impurities. To model the interaction analytically, small intensity modulation interference depth is considered and a perturbation approach is employed. The evolution of the interfering modes is obtained to quantify the interaction. On considering strong pump and

weak signal scenario, it is found that the two SPP modes are coupled by means of the photorefractive effect. The modal gain is calculated to characterize the photorefractive effect. First, an ideal case of lossless waveguides is considered, and the gain versus the waveguide length, the doping concentration and the input amplitudes are characterized. Secondly, the modal losses are taken into account. It is found that a weak antisymmetric mode can experience an effect gain up to certain waveguide lengths in the presence of a strong symmetric mode, considering proper doping concentration and input amplitudes. The coupling effect can be conceived either as an amplification or mode-conversion process, promising novel future application.

The remaining part of this chapter is organized as follows. The propagation modes and the dispersion relation of MIM plasmonic waveguides are introduced in Section 2. The nonlinear and the electro-optical coefficients of the LiNbO_3 are introduced in Section 3. THz generation in nanoplasmonic waveguides is discussed in Section 4. The photorefractive effect in nanoplasmonic waveguides is discussed in Section 5. Finally, concluding remarks are presented in Section 6.

2. MIM Plasmonic waveguides

Consider an MIM plasmonic waveguide comprising two metallic layers sandwiching a LiNbO_3 of thickness a , as depicted in **Figure 1**. The waveguide is two dimensional and independent of the y -axis.

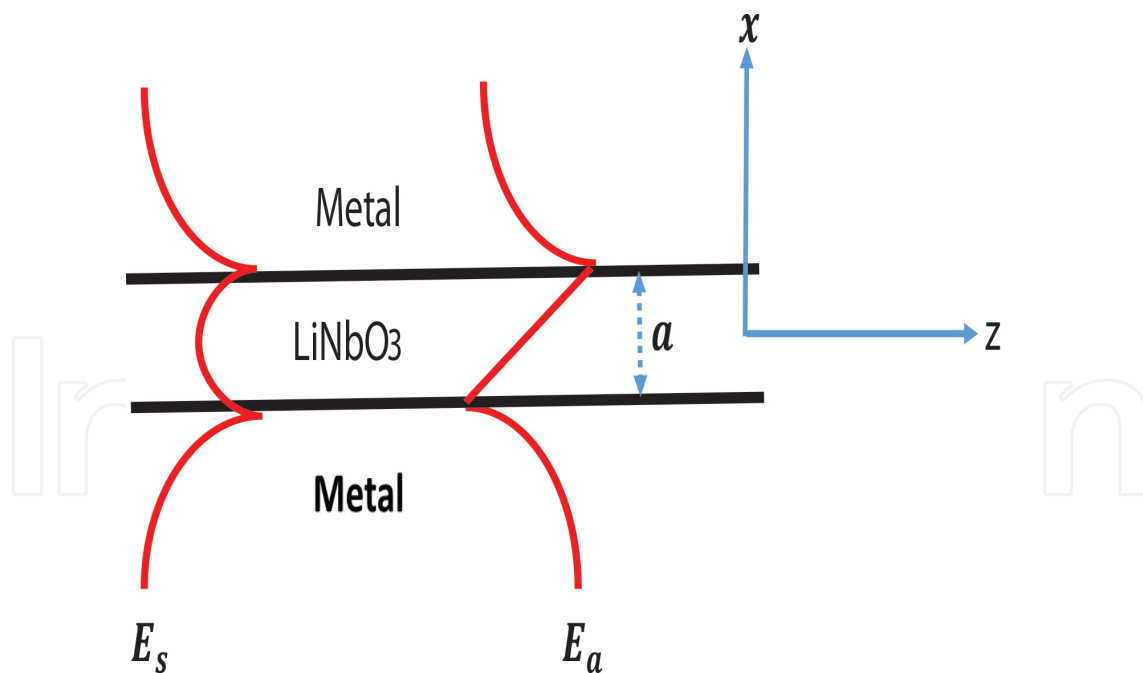


Figure 1. The MIM plasmonic waveguide filled with LiNbO_3 . The spatial distribution of electric field x component is schematically displayed, in red, for both the symmetric and antisymmetric modes.

The waveguide has two fundamental propagating SPP modes of symmetric and antisymmetric transverse field distribution at specific frequency ω , classified according to the spatial

distribution of the x - electric field component. The expression of the electric field associated with the symmetric and antisymmetric modes, i.e. \vec{E}_s and \vec{E}_a , are given by [20]:

$$\begin{aligned}\vec{E}_s(x, z, t) &= A_s(z)[v_x(x)\vec{e}_x + v_z(x)\vec{e}_z]e^{j(\beta_s z - \omega t)} + c.c \\ \vec{E}_a(x, z, t) &= A_a(z)[D_x(x)\vec{e}_x + D_z(x)\vec{e}_z]e^{j(\beta_a z - \omega t)} + c.c\end{aligned}\quad (1)$$

where A_s (and A_a) and β_s (and β_a) are the complex amplitude and propagation constant of the symmetric (and antisymmetric) propagating mode, respectively, $j = \sqrt{-1}$, $c.c.$ is the complex conjugate and $D(z)$ and $v(z)$ are the spatial distributions, given by [20].

$$\begin{aligned}v_x(x) &= \frac{\beta_s}{\omega \epsilon_0 \epsilon_x} \cosh(k_{c_s} x), \quad v_z(x) = \frac{j k_{c_s}}{\omega \epsilon_0 \epsilon_z} \sinh(k_{c_s} x), \\ D_x(x) &= \frac{\beta_a}{\omega \epsilon_0 \epsilon_x} \sinh(k_{c_a} x), \quad D_z(x) = \frac{j k_{c_a}}{\omega \epsilon_0 \epsilon_z} \cosh(k_{c_a} x),\end{aligned}\quad (2)$$

Here, $-\frac{a}{2} < z < \frac{a}{2}$, $\epsilon_{x,z}$ is the LiNbO₃ relative permittivity for x and z polarization, respectively, and $k_{c_{s(a)}} = \sqrt{\frac{\epsilon_x}{\epsilon_x} \beta_{s(a)}^2 - \epsilon_z k_0^2}$ is the core transverse decay factor for the symmetric (and antisymmetric) SPP mode.

On applying the boundary conditions, the dispersion relation for the symmetric and antisymmetric modes can be, respectively, given by the following [20]:

$$\tanh\left(\frac{a}{2} k_{c_s}\right) = -\frac{\epsilon_z k_{m_s}}{\epsilon_m k_{c_s}}, \quad \tanh\left(\frac{a}{2} k_{c_a}\right) = -\frac{\epsilon_m k_{c_a}}{\epsilon_z k_{m_a}},\quad (3)$$

where $k_{m_{s(a)}} = \sqrt{\beta_{s(a)}^2 - \epsilon_m k_0^2}$ is the transverse decay factor in the metal for symmetric (antisymmetric) SPP mode, $k_0 = \frac{2\pi}{\lambda}$ is the propagation constant in the free space, and ϵ_m is the metal permittivity.

One may rewrite the dispersion relation in the following form [18]:

$$\begin{aligned}k_{c_s} \tanh\left(k_{c_s} \frac{a}{2}\right) &= -\frac{\epsilon_z}{\epsilon_m} \left[\frac{\epsilon_x}{\epsilon_z} k_{c_s}^2 + (\epsilon_x - \epsilon_m) k_0^2 \right]^{\frac{1}{2}} \\ k_{c_a} \coth\left(k_{c_a} \frac{a}{2}\right) &= -\frac{\epsilon_z}{\epsilon_m} \left[\frac{\epsilon_x}{\epsilon_z} k_{c_a}^2 + (\epsilon_x - \epsilon_m) k_0^2 \right]^{\frac{1}{2}}\end{aligned}\quad (4)$$

The dispersion form in Eq. (4) can be solved numerically for k_c , for a known frequency ω and slot thickness a . The propagation constant β can then be calculated by $\beta_{s,a}^2 = \frac{\epsilon_x}{\epsilon_z} k_{c_{s,a}}^2 + \epsilon_x k_0^2$.

3. LiNbO₃ coefficients

LiNbO₃ is chosen as the electro-optical material for this work. Consider the indices of the LiNbO₃ (1, 2, 3) along the axes (x, y, z), respectively. Given that the MIM waveguide is

independent of the y -axis, the propagating fields have x and z electric field components, denoted by E_x and E_z . The nonlinear polarization induced in the LiNbO_3 is given by the following [21]:

$$P_{\text{NL}_x} = 4d_{31}E_zE_x, \quad P_{\text{NL}_y} = -2d_{22}E_x^2, \quad P_{\text{NL}_z} = 2d_{31}E_x^2 + 2d_{33}E_z^2, \quad (5)$$

where P_{NL_j} is the J th nonlinear polarization component and $d_{22} = 3 \text{ pm/v}$, $d_{31} = 5 \text{ pm/v}$, and $d_{33} = 33 \text{ pm/v}$ are the nonlinear coefficients. Several phenomena are attributed to the nonlinear polarization, including new frequency generation, frequency conversion and polarization rotation, to mention a few. The evolution of the propagating fields is governed by the nonlinear wave equation that involves the nonlinear polarization. An example of THz generation based on induced nonlinear polarization in MIM nanoplasmonic waveguide is discussed in the next section.

The electro-optic coefficients are related to the nonlinear coefficients by the following:

$$r_{lt} = - \frac{4\pi}{n_x^2 n_z^2} d_{lt}, \quad (6)$$

where n_x and n_z are the principal refractive indices.

The effective permittivity of the LiNbO_3 depends on the electric field components, by means of electro-optic effect, through the following relation [21]:

$$\begin{aligned} \frac{1}{\varepsilon_{x\text{eff}}} &= \frac{1}{\varepsilon_x} + (r_{15} - r_{22})E_x + r_{13}E_z \\ \frac{1}{\varepsilon_{z\text{eff}}} &= \frac{1}{\varepsilon_z} + r_{15}E_x + r_{33}E_z \end{aligned} \quad (7)$$

where ε_{eff} is the effective permittivity of the LiNbO_3 and ε is the intrinsic permittivity of the LiNbO_3 .

On considering a small induced change in the permittivity, so that $(r_{15} - r_{22})E_x + r_{13}E_x \ll \frac{1}{\varepsilon_x}$ and $r_{15}E_x + r_{33}E_x \ll \frac{1}{\varepsilon_z}$, the effective permittivity can be approximated by the following [19]:

$$\begin{aligned} \varepsilon_{x\text{eff}} &= \varepsilon_x - \varepsilon_x^2[(r_{15} - r_{22})E_x + r_{13}E_z], \\ \varepsilon_{z\text{eff}} &= \varepsilon_z + \varepsilon_z^2[r_{15}E_x + r_{33}E_z], \end{aligned} \quad (8)$$

In Section 5, an example of photorefractive effect in MIM plasmonic waveguide based on the electro-optic effect is discussed.

4. THz generation in nanoplasmonic waveguides

In this section, an MIM plasmonic waveguide filled with LiNbO_3 and with two propagating SPP modes is considered. The frequency difference between the two SPP modes is properly designed for THz generation. Theoretical modelling and numerical evaluations are presented.

4.1. Field expressions

As the symmetric mode is a fundamental mode of the MIM waveguides, two symmetric modes with distinct frequencies ω_1 and ω_2 are considered for this work. It then follows that a single mode at each specific frequency can be propagated given a proper waveguide thickness a . The associated electric fields have x and z polarization components, given by the following:

$$\begin{aligned} E_{zi}(x, z, t) &= A_{si}(z) v_{zi}(x) e^{j(\beta_{si}z - \omega_i t)} \vec{e}_z + c.c. \\ E_{xi}(x, z, t) &= A_{si}(z) v_{xi}(x) e^{j(\beta_{si}z - \omega_i t)} \vec{e}_x + c.c. \end{aligned} \tag{9}$$

Here $i \in \{1, 2\}$.

The THz wave is generated by means of difference-frequency generation of the two SPP modes enabled by the LiNbO₃ nonlinearity.

The MIM structure is designed to guide the SPP pumps, whereas the generated THz waves are designed to diffract and propagate outside the MIM waveguide, as shown in **Figure 2**. The thickness of the metallic layer is equal to $d = \frac{5}{k_m}$. It then follows that 99% of the optical SPP modes are confined inside the MIM waveguide, and thus one may conceive the metallic layers to be of infinite thickness. However, because THz waves are of wavelengths much greater than the MIM waveguide dimension, and given that THz waves cannot be guided as SPP modes [22], the generated THz waves will diffract into the surrounding medium and evolve as a Gaussian beam. The generated THz waves can be modelled as a transverse electromagnetic (TEM) Gaussian beam, given by [23] and [24]:

$$E_{THz}(x, z, t) = A_{THz}(z)G(x)e^{j(\beta_3z - \omega_3 t)} \vec{e}_x + c.c, \tag{10}$$

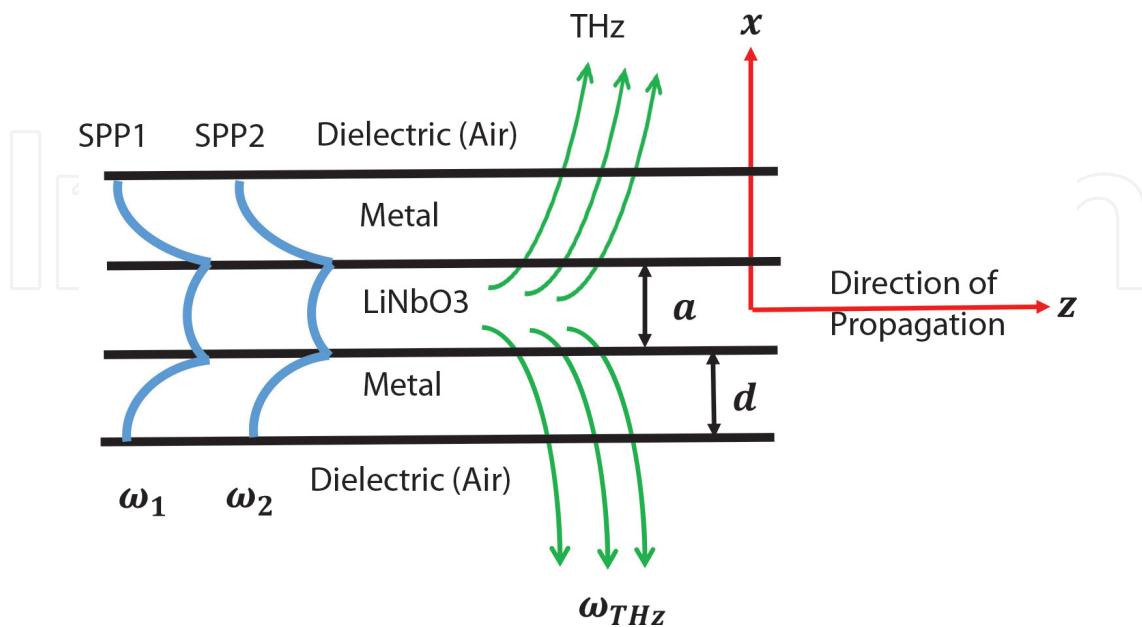


Figure 2. The MIM plasmonic waveguide for THz generation.

where $G(x) = \frac{(2/\pi)^{\frac{1}{4}}}{\sqrt{W_0\gamma(z)}} \exp\left(-\frac{x^2}{\gamma(z)W_0^2}\right)$, A_{THz} is the complex amplitude, W_0 is the beam spot at $z = 0$, $\gamma(z) = 1 + jz/Z_R$, and Z_R is the Rayleigh range given by $\frac{W_0^2\pi}{\lambda}$.

4.2. Nonlinear polarization

The induced nonlinear polarization components are at the frequencies ω_1 , ω_2 , $\omega_1 - \omega_2$, and $\omega_1 + \omega_2$. Here, the frequency difference between the two optical frequencies ω_1 and ω_2 is designed to lie in the THz range. It must be noted that this generated THz wave at $\omega_1 - \omega_2$ cannot be guided by the plasmonic MIM waveguide [22], as previously mentioned. The other generated harmonic at $\omega_1 + \omega_2$ lies in the optical frequency range, close to the second harmonic frequency, and is guided as SPP mode [25]. It then follows that the wave at $\omega_1 + \omega_2$ suffers from strong attenuation. Thus, the nonlinear polarization component at frequency $\omega_1 + \omega_2$ will be ignored in the following analysis. On the substitution of the fields of Eqs. (9) and (10) into Eq. (5), the nonlinear polarization components can be obtained. The nonlinear polarization components at ω_1 are as follows:

$$\begin{aligned} P_{\text{NLz}} &= 4d_{31}A_{s2}A_{\text{THz}}G(x)v_{z2}(x) e^{j[(\beta_{s2}+\beta_{\text{THz}})z-\omega_1t]} \vec{e}_z + c.c., \\ P_{\text{NLx}} &= 4d_{33}A_{s2}A_{\text{THz}}G(x)v_{x2}(x) e^{j[(\beta_{s2}+\beta_{\text{THz}})z-\omega_1t]} \vec{e}_x + c.c., \end{aligned} \quad (11)$$

the nonlinear polarization components at ω_2 are

$$\begin{aligned} P_{\text{NLz}} &= 4d_{31}A_{s1}A_{\text{THz}}^*G^*(x)v_{z1}(x) e^{j[(\beta_{s1}-\beta_{\text{THz}})z-\omega_2t]} \vec{e}_z + c.c., \\ P_{\text{NLx}} &= 4d_{33}A_{s1}A_{\text{THz}}^*G^*(x)v_{x1}(x) e^{j[(\beta_{s1}-\beta_{\text{THz}})z-\omega_2t]} \vec{e}_x + c.c., \end{aligned} \quad (12)$$

and the nonlinear polarization component at $\omega_{\text{THz}} = \omega_1 - \omega_2$ is

$$P_{\text{NLx}} = 4A_{s1}A_{s2}^*[d_{31}v_{z1}v_{z2}^* + d_{33}v_{x1}v_{x2}^*] \times e^{j[(\beta_{s1}-\beta_{s2})z-(\omega_1-\omega_2)t]} \vec{e}_x + c.c., \quad (13)$$

The z -component of the nonlinear polarization at ω_{THz} is not considered because the generated THz wave is a TEM Gaussian wave that propagates in the z -direction. Therefore, the THz wave has a zero z -component electric field. In other words, the x -component of the nonlinear polarization, i.e. P_{NLx} , is the only source that contributes to the evolution of the generated THz wave.

4.3. THz generation

The evolution of the generated THz wave and the SPP modes are governed by the nonlinear wave equation, given by:

$$\nabla^2 E = \mu_0 \epsilon \frac{\partial^2 E}{\partial t^2} + \mu_0 \frac{\partial^2 P_{\text{NL}}}{\partial t^2}, \quad (14)$$

On the substitution of the fields of Eqs. (9) and (10) into Eq. (14), and using the nonlinear polarization expressions of Eqs. (11–13), the corresponding slowly varying envelope approximation (SVEA) equations can be formed, given by the following [18]:

$$\frac{\partial A_{s1}}{\partial z} = j \frac{2 \omega_1^2}{\beta_1 c^2} A_{\text{THz}} A_{s1} \left(d_{31} \frac{\langle v_{z1}/G v_{z2} \rangle}{\langle v_{z1}/v_{z1} \rangle} + d_{33} \frac{\langle v_{x1}/G v_{x2} \rangle}{\langle v_{x1}/v_{x1} \rangle} \right) e^{j(\beta_{s2} + \beta_{\text{THz}} - \beta_{s1})z}, \quad (15)$$

$$\frac{\partial A_{s2}}{\partial z} = j \frac{2 \omega_2^2}{\beta_2 c^2} A_{s1} A_{\text{THz}}^* \left(d_{31} \frac{\langle v_{z2} G/v_{z1} \rangle}{\langle v_{z2}/v_{z2} \rangle} + d_{33} \frac{\langle v_{x2} G/v_{x1} \rangle}{\langle v_{x2}/v_{x2} \rangle} \right) e^{j(\beta_{s1} - \beta_{\text{THz}} - \beta_{s2})z}, \quad (16)$$

$$\frac{\partial A_{\text{THz}}}{\partial z} = j \frac{2 \omega_{\text{THz}}^2}{c^2} A_{s1} A_2^* \frac{d_{31} \langle v_{z2} G/v_{z1} \rangle + d_{33} \langle v_{x2} G/v_{x1} \rangle}{\left(\beta_{\text{THz}} - \frac{1}{2\gamma Y_R} \right) \langle G/G \rangle + \frac{\langle G/z^2 G \rangle}{\gamma^2 W_0^2 Y_R}} e^{j(\beta_{s1} - \beta_{s2} - \beta_{\text{THz}})z}, \quad (17)$$

where $\langle \phi/\delta \rangle = \int_{-\frac{a}{2}}^{+\frac{a}{2}} \phi^*(\zeta) \delta(\zeta) d\zeta$.

The evolution of the THz and the SPP fields can be obtained by numerically solving the SVEA Eqs. (15–17). However, various losses must first be precisely evaluated. These include SPP and THz losses. The decay factor of the SPP linear losses can be calculated from the imaginary part of the propagation constant, i.e. $\alpha_{L_i} = \text{Im}\{\beta_i\}$, by solving Eq. (4). These SPP linear losses can be taken into account by incorporating the corresponding decay factor α_{L_i} in the SVEA Eqs. (15) and (16). The SPP nonlinear losses are described by the decay factor α_{NL} , given by $\alpha_{NL} = \gamma_{NL} I$ [26]. Here, $\gamma_{NL} = 2.7 \times 10^{-5}$ m/W is the nonlinear absorption coefficient of LiNbO₃ crystal, and I is the power of the SPP modes. Our investigations show that the nonlinear losses in this work are much smaller than the linear losses, and can be ignored despite the large SPP intensities because the waveguide lengths considered in this work are very small and lie in the micrometer range. However, the THz losses are also mainly linear, given the low generated intensities. The effective decay factor of the THz losses is given by the following:

$$\alpha_{\text{THz}} = \left(\alpha_{\text{THz}_{\text{LN}}} \int_{-\frac{a}{2}}^{+\frac{a}{2}} G(x) dx + 2\alpha_{\text{THz}_{\text{Metal}}} \int_{\frac{a}{2}}^{d+\frac{a}{2}} G(x) dx \right) / \int_{-W}^{+W} G(x) dx, \quad (18)$$

where $\alpha_{\text{THz}_{\text{Metal}}}$ is the metal THz absorption coefficient, $\alpha_{\text{THz}_{\text{LN}}}$ is the LiNbO₃ THz absorption coefficient and W is the Gaussian beam spot given by $W = W_0 \sqrt{1 + \left(\frac{z}{z_R}\right)^2}$. To take the THz losses into account, one must incorporate the effective THz decay factor of Eq. (18) into the SVEA Eq. (17). Experimental values of metal and LiNbO₃ absorption coefficients can be found in the literature. For example, in [27] the absorption coefficient of gold is given by $\alpha_{\text{THz}_{\text{Metal}}} = 6 \times 10^6 \text{ m}^{-1}$, and in [28] the absorption coefficient of the LiNbO₃ is given by $\alpha_{\text{THz}_{\text{LN}}} = 2 \times 10^4 \text{ m}^{-1}$, both for the 4 THz frequency. It must be noted that the total THz losses are minimized in this work, as can be inferred from Eq. (18). This is because the generated THz waves diffract rapidly to propagate outside of the MIM plasmonic waveguide even for a

few 10's of nanometers of propagation. For instance, considering a 4 THz wave, the beam spot evolves from 120 nm (which is the slot thickness, i.e. a) to approximately 10 μm by propagating only 50 nanometers.

4.4. Numerical evaluations

In the following analysis, we consider gold for the two metallic layers, a slot thickness of $a = 120$ nm, a metal thickness of $d = 110$ nm and $A_{s1}(0) = A_{s2}(0) = 1$ V/ μm . In **Figure 3**, the power of a 4 THz generated wave is shown versus the waveguide length. Here, $\lambda_1 = 1550$ nm and $\lambda_2 = 1582$ nm. The power is calculated per unit width, defined by $p_i = \frac{1}{2} \varepsilon_0 c n_i |A_{si}|^2 \int_{-\infty}^{+\infty} v_i v_i^* dx$ and $p_{\text{THz}} = \frac{1}{2} \varepsilon_0 c n_{\text{THz}} |A_{\text{THz}}|^2 \int_{-\infty}^{+\infty} G G^* dx$, where the SPP power is $p_1 + p_2$.

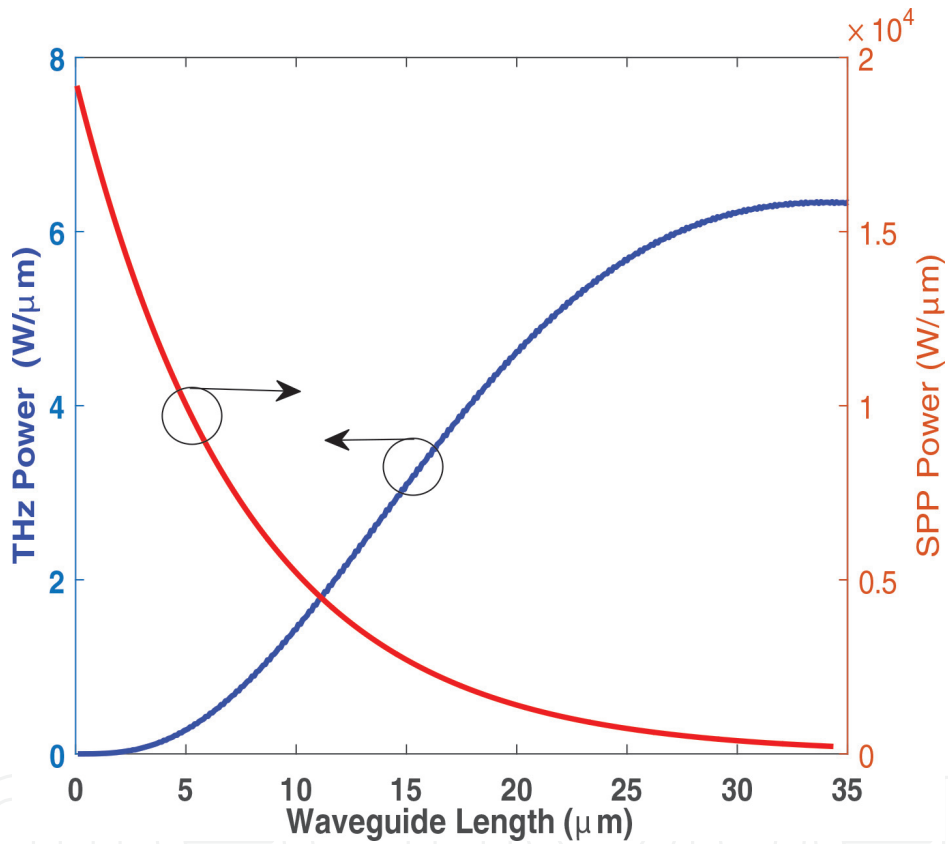


Figure 3. Power of the generated 4 THz wave, and SPPs power versus waveguide length.

As can be seen in **Figure 3**, the effective waveguide length is limited to 35 μm and most of the SPP power is dissipated by losses.

The optics-to-THz conversion efficiency can be defined as $\eta = \frac{p_{\text{THz}}(L)}{p_1(0)+p_2(0)}$, where $p_{\text{THz}}(L)$ is the THz power per unit width, L is the MIM waveguide length, and $p_{1,2}(0)$ is the input SPP powers per unit width.

In **Figure 4**, the conversion efficiency for a 4 THz generated wave is presented versus the input SPP power. Here, we consider a waveguide length of $L = 35$ μm , $\lambda_1 = 1550$ nm and

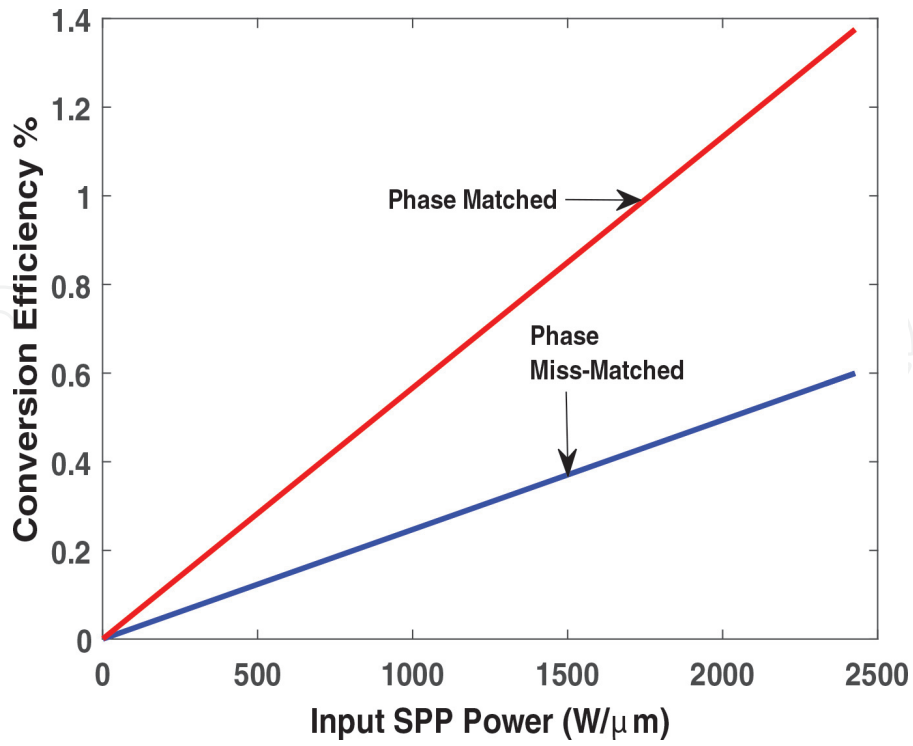


Figure 4. Conversion efficiency for a 4 THz wave versus total SPP input power. The two scenarios of phase matching and phase mismatching are shown for comparison.

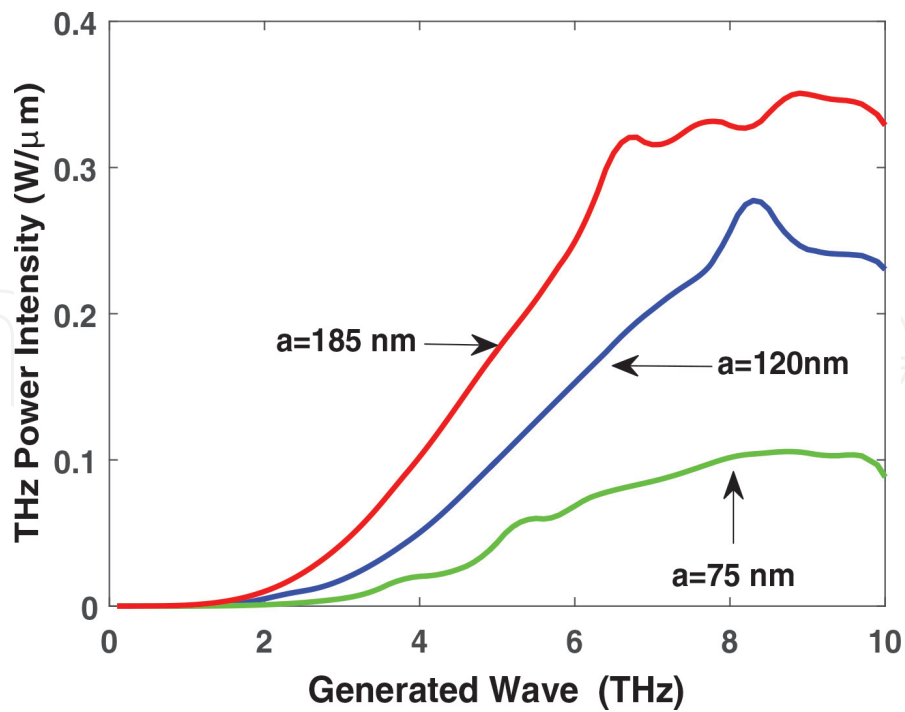


Figure 5. Power of the generated THz wave versus its frequency. Different slot thicknesses are considered. The optical wavelength λ_1 is fixed at the value $\lambda_1 = 1550$ nm. The waveguide length is $L = 35$ μm.

$\lambda_2 = 1582$ nm. Additionally, a hypothetical case of phase-matched generation is presented (by setting $\beta_1 - \beta_2 - \beta_{\text{THz}} = 0$) for comparison. As can be seen, the phase-matching enhancement is maximally approximately 4 THz because the interaction is limited by losses. For instance, for 4 THz generation and $\lambda_1 = 1550$ nm, the beat length L_B (defined by $L_B = \frac{2\pi}{\beta_{s1} - \beta_{s2} - \beta_{\text{THz}}}$) is approximately 42 μm , whereas the SPP propagation length (defined by $L_{\text{SPP}} = (2\alpha)^{-1}$) is approximately 25 μm . Thus, it is intuitive to expect limited enhancement of phase-matched operation.

The frequency of the generated THz wave can be tuned by controlling the frequency difference between the two SPP modes, i.e. $f_1 - f_2$. In **Figure 5**, the wavelength 1 is fixed at $\lambda_1 = 1550$ nm, whereas wavelength 2 is tuned to generate different THz wave frequencies from 1 to 10 THz. As can be seen from **Figure 5**, THz waves can be generated over the entire range from 1 to 10 THz simply by tuning the frequency ω_2 . Furthermore, different slot waveguide thicknesses are considered in **Figure 5**. These include $a = 75$, $a = 120$ and $a = 185$ nm. It can be seen that, for the same SPP input, smaller slot thickness result in weaker generated THz waves. This is due to higher losses for smaller slot thickness. Thus, as expected, more compact generation is achieved at the cost of higher losses.

5. Photorefractive effect in nanoplasmonic waveguides

In this section, the LiNbO_3 filling the MIM waveguide is doped with N_D donor and N_A acceptor atom impurities. The interaction between two (symmetric and antisymmetric) interfering SPP modes is studied.

5.1. Intensity expression

The electric fields of the two symmetric and antisymmetric propagating modes are described by Eq. (1). The optical field intensity inside of the waveguide, $I = (\vec{E}_s + \vec{E}_a)(\vec{E}_s^* + \vec{E}_a^*)$, can be formed as follows:

$$I(x, z, t) = I_0(x) + \text{Re}\{I_1(x)e^{j\Delta\beta z}\} \quad (19)$$

where $\Delta\beta = \beta_a - \beta_s$, $I_0(x, z) = T_1(x)|A_a(z)|^2 + T_2(x)|A_s(z)|^2$, $I_1(x, z) = T_3(x) A_a(z) A_s^*(z)$, $T_1(x) = D_x(x) D_x^*(x) + D_z(x) D_z^*(x)$, $T_2(x) = v_x(x) v_x^*(x) + v_z(x) v_z^*(x)$, and $T_3(x) = 2D_x(x) v_x(x) + 2D_z(x) v_z(x)$.

On adapting a strong pump and weak signal scenario, i.e. $I_1 \ll I_0$, a perturbation approach can be implemented to model the evolution of the propagating fields.

5.2. Band transport model

The interaction of the interfering SPP modes with LiNbO_3 impurities is governed by the standard band transport model that encompasses the electron continuity equation, the current density equation and the Poisson's equation, as in the following [29]:

$$\frac{\partial N}{\partial t} - \frac{\partial N_D^i}{\partial t} = \frac{1}{e} \nabla \cdot (J), \quad (20)$$

$$\frac{\partial N_D^i}{\partial t} = (N_D - N_D^i)SI - \gamma_R NN_D^i, \quad (21)$$

$$\nabla \cdot \epsilon E_{SC} = -e(N + N_A - N_D^i), \quad (22)$$

where N is the free electron density, N_D^i is the ionized donor density, e is the electron charge, $J = eN\mu E_{SC} + k_B T \mu \nabla N + \kappa(N_D - N_D^i)SI\hat{e}_z$ is the conduction current density, μ is the LiNbO₃ electron mobility, k_B is the Boltzmann constant, T is the temperature, κ is the photovoltaic constant, E_{SC} is the space charge electric field, and ϵ is the LiNbO₃ permittivity. The three coupled equations of the band transport model shown above can be solved analytically by obeying a perturbation approach for a small depth intensity modulation limit i.e. $I_0 \gg I_1$. Towards solving these three coupled equations (20)–(22) for a continuous wave case, and considering small intensity modulation, the electron density N and the ionized donor density N_D^i can be written in the following form:

$$\begin{aligned} N_D^i(x, z) &= N_{D0}^i(x) + \text{Re}\left(N_{D1}^i(x) e^{j\Delta\beta z}\right) \\ N(x, z) &= N_0(x) + \text{Re}\left(N_1(x) e^{j\Delta\beta z}\right) \end{aligned} \quad (23)$$

where N_0 and N_{D0}^i are the averages of electron and ionized donor densities, and N_1 and N_{D1}^i are the modulation amplitudes of electron and ionized donor densities, respectively.

The space charge electric field E_{SC} can be uniquely specified through Eq. (22) and the electrostatic condition, i.e. $\nabla \times E_{SC} = 0$.

Consequently, on substituting Eq. (23) into Eq. (22), and using the electrostatic condition, one can obtain the following expression [19]:

$$E_{SC}(x, z) = c_{SC}[N_1 - N_{D1}^i]e^{j\Delta\beta z}\vec{e}_z + \frac{c_{SC}}{j\Delta\beta} \frac{\partial[N_1 - N_{D1}^i]}{\partial x} e^{j\Delta\beta z}\vec{e}_x + c.c., \quad (24)$$

Where $c_{SC} = \frac{-ej\Delta\beta}{\epsilon_0\epsilon_x(k_{cs} + k_{ca})^2 + \epsilon_0\epsilon_z(j\Delta\beta)^2}$

By substituting Eq. (23) into Eqs. (20) and (21), and considering a steady state so that the time rates of the free electrons and the ionized donor densities are zeros (i.e. $\frac{\partial N}{\partial t} = \frac{\partial N_D^i}{\partial t} = 0$) [29], the expressions for N_0 , N_{D0}^i , N_1 and N_{D1}^i can be obtained. First, by substituting Eq. (23) in Eqs. (20) and (21), equating the average terms, and using $N_0 + N_A - N_{D0}^i = 0$, one obtains the following:

$$N_0 = \frac{-(N_A\gamma_R + SI_0) + \sqrt{(N_A\gamma_R + SI_0)^2 + 4\gamma_R SI_0(N_D - N_A)}}{2\gamma_R}, \quad (25)$$

$$N_{D0}^i = \frac{(N_A\gamma_R - SI_0) + \sqrt{(N_A\gamma_R + SI_0)^2 + 4\gamma_R SI_0(N_D - N_A)}}{2\gamma_R}, \quad (26)$$

Secondly, by substituting Eq. (23) into Eqs. (20) and (21) and equating the modulation terms (i.e. those with $e^{j\Delta\beta z}$), one obtains:

$$N_1(x) = \frac{a_1 b_2 + a_2 b_3}{a_3 b_2 - a_2 b_1} I_1(x), \quad (27)$$

$$N_{D1}^i(x) = \frac{a_1 b_1 + a_3 b_3}{a_2 b_1 - a_3 b_2} I_1(x), \quad (28)$$

where $a_1 = s(N_D - N_{D0}^i)$, $a_2 = N_0 \gamma_R + SI_0$, $a_3 = N_{D0}^i \gamma_R$, $b_1 = \mu \left((k_{c_s} + k_{c_a})^2 + (j\Delta\beta)^2 \right) \times \left(k_B T - \frac{e^2 N_0}{\epsilon_0 \epsilon_x (k_{c_s} + k_{c_a})^2 - \epsilon_0 \epsilon_z (j\Delta\beta)^2} \right)$, $b_2 = -\kappa s (j\Delta\beta)^2 + \frac{e^2 N_0 \mu \left((k_{c_s} + k_{c_a})^2 + (j\Delta\beta)^2 \right)}{\epsilon_0 \epsilon_x (k_{c_s} + k_{c_a})^2 - \epsilon_0 \epsilon_z (j\Delta\beta)^2}$ and $b_3 = \kappa s (N_D - N_{D0}^i) (j\Delta\beta)$.

The spatial electric field E_{SC} can be evaluated by performing the following three steps. First, one must calculate the average electron and ionized donor densities, i.e. N_0 and N_{D0}^i , using Eqs. (25) and (26). Secondly, the modulation amplitudes of electron and ionized donor densities, i.e. N_1 and N_{D1}^i , can be calculated using Eqs. (27) and (28). Finally, the E_{SC} can be evaluated by using Eq. (24). The spatial electric field modifies the effective permittivity of the MIM waveguide, by means of electro-optic effect, causing the SPP modes to be coupled in a phase-matched fashion, a phenomenon known as the photorefractive effect.

5.3. Photorefractive effect

The evolution of the SPP modes are governed by nonlinear wave equation, given by:

$$\nabla^2 \vec{E} - \frac{1}{\epsilon_0 c} \frac{\partial^2 \vec{D}}{\partial t^2} = 0, \quad (29)$$

where \vec{D} is the displacement current given by $\vec{D} = \epsilon_0 \epsilon_{\text{eff}} \vec{E}$.

The effective permittivity can be obtained by substituting the spatial electric field, i.e. E_{SC} , of Eq. (24) into Eq. (8), yielding the following:

$$\begin{aligned} \epsilon_{x\text{eff}} &= \epsilon_x - \epsilon_x^1 e^{j\Delta\beta} + c.c, \\ \epsilon_{z\text{eff}} &= \epsilon_z - \epsilon_z^1 e^{j\Delta\beta} + c.c, \end{aligned} \quad (30)$$

where $\epsilon_x^1 = (\epsilon_x)^2 \left(r_{13} c_{sc} (N_1 - N_{D1}^i) + (r_{15} - r_{22}) \frac{c_{sc}}{j\Delta\beta} \frac{\partial(N_1 - N_{D1}^i)}{\partial x} \right)$, and $\epsilon_z^1 = (\epsilon_z)^2 \left(r_{33} c_{sc} (N_1 - N_{D1}^i) + r_{15} \frac{c_{sc}}{j\Delta\beta} \frac{\partial(N_1 - N_{D1}^i)}{\partial x} \right)$

On the substitution of symmetric and antisymmetric mode expressions of Eq. (1) into Eq. (29) and using Eq. (30), the fields equations (for slowly varying amplitudes) can be obtained, given by the following [19]:

$$\frac{\partial A_s}{\partial z} + \frac{(j\omega)^2 C_1^*}{j8c^2 \beta_s} \left(r_{33} \epsilon_z^2 \frac{k_{c_a}}{k_{c_s}} - r_{13} \epsilon_x^2 \frac{\beta_a}{\beta_s} \right) |A_s|^2 A_s = 0, \quad (31)$$

$$\frac{\partial A_a}{\partial z} + \frac{(j\omega)^2 C_1}{j8c^2 \beta_a} \left(r_{13} \epsilon_x^2 \frac{\beta_s}{\beta_a} - r_{33} \epsilon_z^2 \frac{k_{c_s}}{k_{c_a}} \right) |A_s|^2 A_a = 0, \quad (32)$$

Where $c_1 = \frac{-2e\Delta\beta}{\epsilon_0 \epsilon_x (k_{c_s} + k_{c_a})^2 + \epsilon_0 \epsilon_z (j\Delta\beta)^2} \left(\frac{N_1}{I_1} - \frac{N_{D1}^i}{I_1} \right) \left(\frac{\beta_a \beta_s}{(\omega \epsilon_0 \epsilon_x)^2} - \frac{k_{c_s} k_{c_a}}{(\omega \epsilon_0 \epsilon_z)^2} \right)$,

As can be seen in Eqs. (31) and (32), the two SPP modes are coupled in a phase-matched fashion. The coupling is conducted by the spatial space charge electric field generated by the interfering SPP modes in the doped LiNbO₃. This is known as the photorefractive effect. The photorefractive effect has been known since the early 1960s [30] in bulk materials and micrometer dielectric waveguides. In this work, the photorefractive effect is investigated in nanoplasmonic waveguides. Numerical evaluations are presented in the following section.

5.4. Numerical evaluations

To illustrate the potential of the photorefractive effect in plasmonic waveguides, typical realistic values are considered. Consider $r_{13} = 11 \text{ pm/V}$, $r_{33} = 34 \text{ pm/V}$, $T = 300\text{K}$, $\mu = 7.4 \times 10^{-5} \text{ m}^2/(\text{V}\cdot\text{s})$, $S = 2.34 \times 10^{-8} \text{ m}^2/(\text{s}\cdot\text{V}^2)$, $\kappa = 1.5 \times 10^{11} (\text{m/V})$ and $\gamma_R = 2.4 \times 10^{-13} \text{ m}^3/\text{s}$ [29, 31, 32]. In this work, the blue wavelength $\lambda = 458 \text{ nm}$ is considered, given its known functionality in photorefractive devices. The LiNbO₃ permittivity is $\epsilon_z = 5.177$ and $\epsilon_x = 5.624$ at this wavelength. Also, the aluminium metal (i.e. Al) is chosen as the cladding material, that has a permittivity of $\epsilon_m = -29 + 7j$ at $\lambda = 458 \text{ nm}$.

First, the waveguide losses are ignored and the gain versus the doping concentration and the input amplitudes is characterized. Different slot thicknesses are considered. Secondly, the modal losses are taken into account, considering proper doping concentration and input amplitudes.

Our numerical investigations show that gain can be realized only for weak antisymmetric mode (the signal) co-propagating with strong symmetric mode (the pump). This is because the space charge electric field, that couples the two modes, has an antisymmetric transverse distribution, as can be inferred from Eqs. (2), (19) and (24).

In **Figure 6**, the antisymmetric gain, defined by $A_a(L)/A_a(0)$, is displayed versus the waveguide length L in (a), the doping concentration N_D in (b), the inputs ratio $A_a(0)/A_s(0)$ in (c) and the input pump amplitude $A_s(0)$ in (d). The modal losses are ignored and three different thicknesses (i.e. $a = 50 \text{ nm}$, $a = 70 \text{ nm}$ and $a = 90 \text{ nm}$) are considered. In (a), $|A_a(0)| = 0.001 \times |A_s(0)|$ and $N_D = 12 \times 10^{20} \text{ m}^{-3}$. In (b), the waveguide length $L = 84 \text{ }\mu\text{m}$, $|A_s(0)| = 1.935 \times 10^3 (\text{V/m})$, and $|A_a(0)| = 0.001 \times |A_s(0)|$. In (c), the waveguide length $L = 84 \text{ nm}$, $N_D = 12 \times 10^{20} \text{ m}^{-3}$. In (d), the waveguide length $L = 84 \text{ nm}$, $N_D = 12 \times 10^{20} \text{ m}^{-3}$ and $A_a(0)/A_s(0) = 10^{-3}$.

As can be seen from the simulations in **Figure 6**, the photorefractive response, characterized by the gain, is qualitatively the same for different waveguide thicknesses, given losses are ignored. However, it can be seen from part (b) that the gain crucially depends on the doping concentration; the stronger the effect, the larger the doping concentration. Furthermore, it can be seen from part (c) that the gain does not dramatically depend on the input ratio, given that the perturbation condition is satisfied, i.e. $A(0)_a/A(0)_s \leq 1$. Finally, it can be seen from part (d) that the gain is crucially depending on the pump input amplitude (i.e. the symmetric mode input amplitude); the stronger the effect, the larger the input amplitude. These properties characterize the photorefractive effect considering ignored losses. Same properties are expected for fields propagating few micrometers of waveguide length. However, for larger waveguide lengths, such as 10's or 100's of micro-meters, altered characteristics are expected, given that losses are dominating for such waveguide length ranges [19].

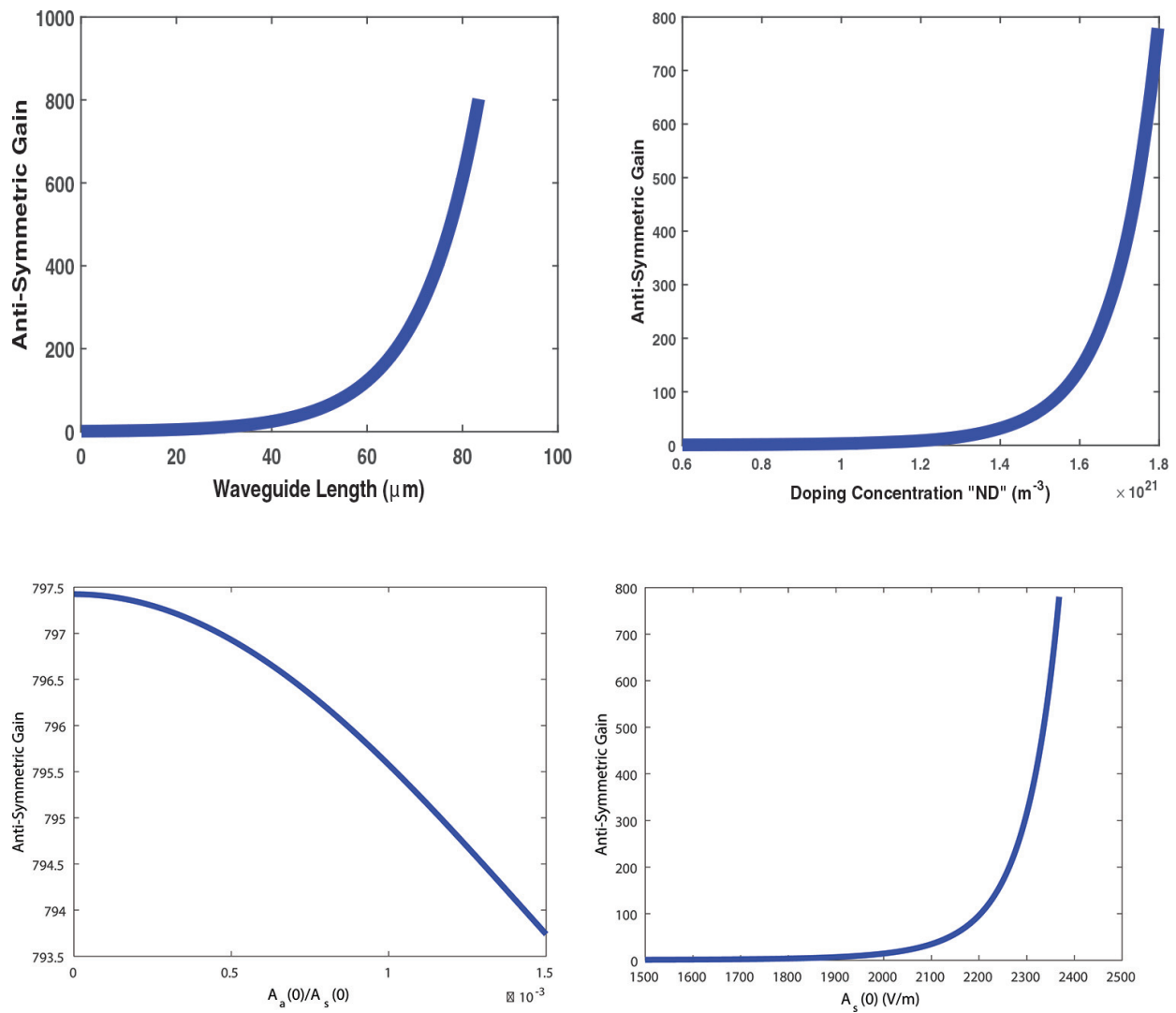


Figure 6. The antisymmetric gain (a) versus waveguide length; (b) versus the doping concentration N_D ; (c) versus the input ratio $\frac{A_a(0)}{A_s(0)}$ and (d) versus the input pump field amplitude $A_s(0)$.

Losses can be taken into account by incorporating the effective decay factor, given by $\alpha_{\text{eff},a} = \text{Im}\{\beta_{s,a}\}$, in Eqs. (31) and (32).

In **Figure 7**, the antisymmetric gain is presented against the waveguide length. Here, losses are taken into account. Three different thicknesses of $a = 50$ nm, $a = 70$ nm and $a = 90$ nm are considered with input pump amplitudes of 4.7×10^3 (V/m), 16.5×10^3 (V/m), and 18.4×10^3 (V/m) are presumed, respectively. The input pump amplitudes are chosen so that the maximum gain is identical for the three thicknesses for the purpose of comparison. As can be seen in **Figure 7**, a significant gain can be experienced despite losses with the maximum gain attainable at the same waveguide length $L = 1.1$ μm . However, a net gain is experienced up to different waveguide lengths for different thicknesses. This is because the photorefractive effect dominates the interaction for the first few micro-meters, whereas losses limit the interaction for larger waveguide lengths, with greater antisymmetric losses for larger waveguide thicknesses.

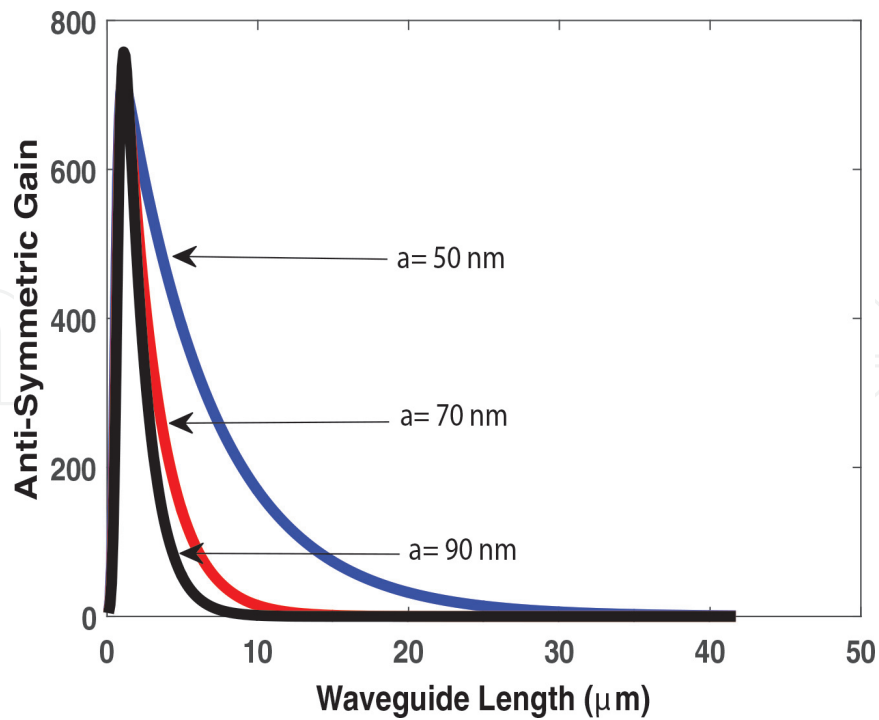


Figure 7. The antisymmetric gain versus waveguide length, for three different LiNbO_3 thicknesses, taking losses into account.

Figure 8 depicts the results of **Figure 7** in dB units. As can be seen, given the assumed parameters, the maximum achieved gain can be 28.8 dB for the three different thicknesses. It can also be seen that for different waveguide thicknesses, the photorefractive gain compensate losses up to different waveguide lengths. For instance, the zero dB gain can be achieved at waveguide lengths of $L = 41 \mu\text{m}$, $L = 16.2 \mu\text{m}$ and $L = 10.6 \mu\text{m}$ for waveguide thicknesses of

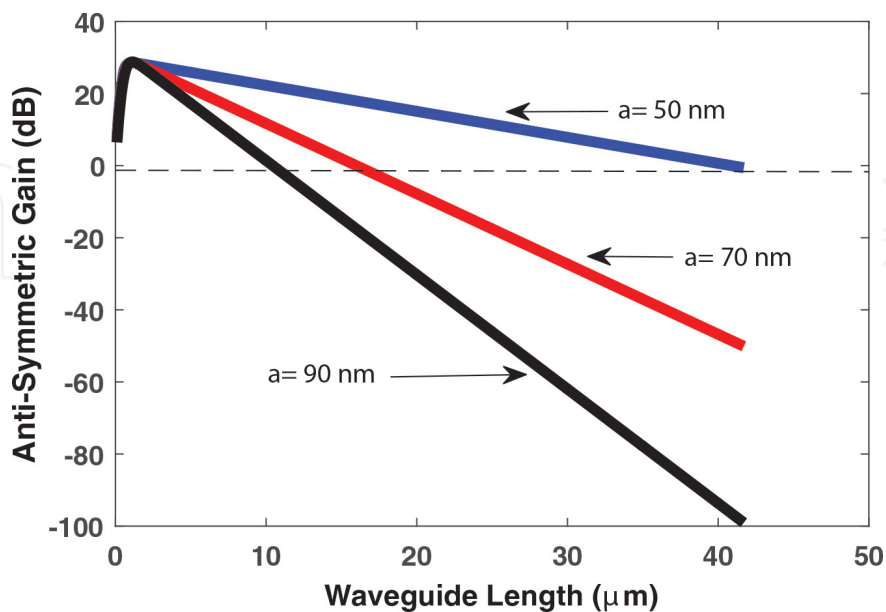


Figure 8. The antisymmetric gain in dB versus waveguide length, taking losses into account.

$a = 50$ nm, $a = 70$ nm and $a = 90$ nm, respectively, for the same reason mentioned above explained by having greater antisymmetric losses for larger waveguide thicknesses.

6. Conclusion

Nanoplasmonic waveguides filled with electro-optical material were proposed and discussed. The aim of this work is to incorporate the unique properties of plasmonic waveguides, ultra-compact structures and high internal intensities, with electro-optical material properties, thus achieving novel functionalities. Two configurations were chosen and investigated. First, an Au-LiNbO₃-Au nanostructure waveguide is considered for THz generation by means of difference-frequency generation of SPP modes. The SPP modes are designed to be totally confined inside the waveguide, whereas the generated THz waves are concentric with the SPP modes and contained mainly in the surrounding medium of the waveguide. Several advantages are achieved through this design. First, THz losses are minimized. Secondly, an off-resonance operation is conducted. Finally, a nanoscale and yet simple THz generation is offered. The evolution of the THz wave and the SPP modes are evaluated and found to be mainly limited by losses. Nevertheless, THz generation is shown to be viable over the entire range from 1 to 10 THz by properly designing the SPP wavelengths and waveguide dimension. Possible future applications include nanocommunication systems and body-centric networks. Secondly, an AL-LiNbO₃-AL nanostructure is considered with the LiNbO₃ being doped with donor and acceptor atom impurities. Two SPP modes with symmetric and antisymmetric spatial distribution are considered. The interaction of the interfering SPP modes with the atom impurities is modelled. It was found that the SPP modes are coupled by the means of the photorefractive effect. A net gain was shown viable for weak antisymmetric mode co-propagating with strong symmetric mode. The antisymmetric gain was studied against the doping concentration and the input amplitudes. This work opens up new opportunities to apply known photorefractive applications to nanoplasmonic devices. The two configurations discussed in this chapter demonstrate the potential of utilizing electro-optical materials in nanoplasmonic waveguides to achieve novel, efficient and ultra-compact devices.

Acknowledgement

This work was supported by the Centre on Smart Service for Smart Cities at Abu Dhabi University, UAE, under grant 19300066.

Author details

Montasir Qasymeh

Address all correspondence to: montasir.qasymeh@adu.ac.ae

Department of Electrical and Computer Engineering, Abu Dhabi University, UAE

References

- [1] E. Ozbay. Plasmonic: Merging photonics and electronics at nanoscale dimensions. *Science*. 2006; **311**(5758):189–193.
- [2] D. K. Gramotnev, and S. I. Bozhevolnyi. Plasmonics beyond the diffraction limit. *Nature Photon*. 2010; **4**:83–91.
- [3] J. A. Schuller, E. S. Barnard, W. Cai, Y. C. Jun, J. S. White, and M. L. Brongersma. Plasmonics for extreme light concentration and manipulation. *Nature Materials*. 2010; **9**:193–204.
- [4] N. Pleros, E. E. Kriezis, and K. Vysokinos. Optical interconnects using plasmonics and si-photonics. *IEEE Photonics Journal*. 2011; **3**(2):296–301.
- [5] D.-S. Ly-Gagnon, K. C. Balram, J. S. White, P. Wahl, M. L. Brongersma, and D. A. B. Miller. Routing and photodetection in subwavelength plasmonic slot waveguides. *Nanophotonic*. 2012; **1**:9–16.
- [6] K. F. MacDonald, Z. L. Samson, M. I. Stockman, and N. I. Zheludev. Ultrafast active plasmonics. *Nature Photon*. 2009; **3**:55–58.
- [7] S. Yue, J. Chen, and Q. Gong. Ultrasmall and ultrafast all-optical modulation based on a plasmonic lens. *Applied Physics Letter*. 2011; **98**:#1611108.
- [8] J. N. Caspers, N. Rotenberg, and H. M. Van Driel. Ultrafast silicon-based active plasmonics at telecom wavelengths. *Optics Express*. 2010; **18**(19):19761–19769.
- [9] M. Cohen, Z. Zalevsky, and R. Shavit. Towards integrated nanoplasmonic logic circuitry. *Nanoscale*. 2013; **5**(12):5442–5449.
- [10] W. Cai, A. P. Vasudev, and M. L. Brongersma. Electrically controlled nonlinear generation of light with plasmonics. *Science*. 2011; **333**:1720–1723.
- [11] P. Berini, and I. D. Leon. Surface plasmon-polariton amplifiers and lasers. *Nature Photon*. 2011; **6**(1):16–24.
- [12] J. Xiang, E. Cassan, D. Gao, and X. Zhang. Highly efficient phase-matched second harmonic generation using an asymmetric plasmonic slot waveguide configuration in hybrid polymer-silicon photonics. *Optics Express*. 2013; **21**(12):14876–14887.
- [13] M. Z. Alam, J. Stewart Aitchison, and M. Mojahedi. Compact and silicon-on-insulator-compatible hybrid plasmonic TE-pass polarizer. *Optics Letters*. 2012; **37**(1):55–57.
- [14] M. C. Schaafsma, H. Starmans, A. Berrier, and J. Gómez Rivas. Enhanced terahertz extinction of single plasmonic antennas with conically tapered waveguides. *New Journal of Physics*. 2013; **15**(1):#015006.

- [15] A. Joushaghani, B. A. Kruger, S. Paradis, D. Alain, S. Aitchison, and J. K. S. Poon. Sub-volt broadband hybrid plasmonic-vanadium dioxide switches. *Applied Physics Letters*. 2013; **102**:#161101.
- [16] J.-Y. Yan, L. L., and J. Xiao. Ring-like solitons in plasmonic fiber waveguides composed of metal-dielectric multilayers. *Optics Express*. 2012; **20**(3):1945–1952.
- [17] X.-T. Kong, Z.-B. Li, and J.-G. Tian. Mode converter in metal-insulator-metal plasmonic waveguide designed by transformation optics. *Optics Express*. 2013; **21**(8):9437–9446.
- [18] M. Qasymeh. Terahertz generation in nonlinear plasmonic waveguides. *IEEE Journal of Quantum Electronics*. 2016; **52**(4):#8500207.
- [19] M. Qasymeh. Photorefractive Effect in Plasmonic Waveguides. *IEEE Journal of Quantum Electronics*. 2014; **50**(5):327–333.
- [20] J. Park, K.-Y. Kim, I.-M. Lee, H. Na, S.-Y. Lee, and B. Lee. Trapping light in plasmonic waveguides. *Optics Express*. 2010; **18**(2):598–623.
- [21] K. K. Wong. *Properties of Lithium Niobate*. London, UK: INSPEC. 2002.
- [22] D. Martin-Cano, M. L. Nesterov, A. I. Fernandez-Dominguez, F. J. Garcia-Vidal, L. Martin-Moreno, and E. Moreno. Domino plasmons for subwavelength terahertz circuitry. *Optics Express*. 2010; **18**(2):754–764.
- [23] J. C. Gutierrez-Vega. Fractionalization of optical beams: I. Planar analysis. *Optics Letters*. 2007; **32**(11):1521–1523.
- [24] M. A. Bandres and J. C. Gutierrez-Vega. Cartesian beams. *Optics Letter*. 2001; **32**(23):3459–3461.
- [25] Y. Sun, Z. Zheng, J. Cheng, G. Sun, and G. Qiao. Highly efficient second harmonic generation in hyperbolic metamaterial slot waveguides with large phase matching tolerance. *Optics Express*. 2015; **23**(5):6370–6378.
- [26] S. M. Kostritskii, and M. Aillerie. Z-scan study of nonlinear absorption in reduced LiNbO₃ crystals. *Journal of Applied Physics*. 2012; **111**:#103504.
- [27] H. Yasuda, and I. Hosako. Measurement of terahertz refractive index of metal with terahertz time-domain spectroscopy. *Japanese Journal of Applied Physics*. 2008; **47**(3):1632–1634.
- [28] M. Unferdorben, Z. Szaller, I. Hajdara, J. Hebling, and L. Pálfalvi. Measurement of refractive index and absorption coefficient of congruent and stoichiometric lithium niobate in the terahertz range. *Journal of Infrared Milli. Terahz. Waves*. 2015; **36**(12):1203–1209.
- [29] P. Yeh. *Introduction to Photorefractive Nonlinear Optics*. New York, NY: Wiley; 1993.

- [30] A. Ashkin, G. D. Boyd, J. M. Dziedzic, R. G. Smith, A. A. Ballman, J. J. Levinstein and K. Nassau. Optically induced refractive index inhomogeneities in LiNbO_3 and LiTaO_3 . *Applied Physics Letters*. 1966; **9**(1):72–74.
- [31] Y. Yang, and D. Psaltis. Photorefractive properties of lithium niobate crystals doped with manganese. *Journal of Optical Society of America B*. 2003; **20**(7):1491–1502.
- [32] Y. Furukawa, K. Kitamura, S. Takekawa, K. Niwa, and H. Hatona. Stoichiometric Mg: LiNbO_3 as an effective material for nonlinear optics. *Optics Letters*. 1998; **23**(24):1892–1894.

IntechOpen